Accepted Manuscript

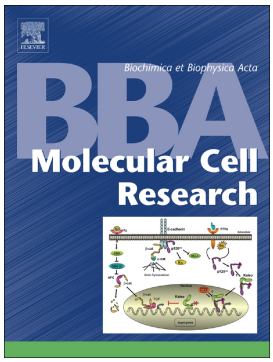

Doublecortin X (DCX) serine 28 phosphorylation is a regulatory switch, modulating association of DCX with microtubules and actin filaments

Maryam Moslehi, Dominic C.H. Ng, Marie A. Bogoyevitch

PII: S0167-4889(18)30307-0
DOI: https://doi.org/10.1016/j.bbamcr.2019.01.003
Reference: BBAMCR 18422

To appear in: *BBA - Molecular Cell Research*

Received date: 28 August 2018
Revised date: 17 December 2018
Accepted date: 4 January 2019

Please cite this article as: Maryam Moslehi, Dominic C.H. Ng, Marie A. Bogoyevitch , Doublecortin X (DCX) serine 28 phosphorylation is a regulatory switch, modulating association of DCX with microtubules and actin filaments. Bbamcr (2019), https://doi.org/10.1016/j.bbamcr.2019.01.003

Doublecortin X (DCX) serine 28 phosphorylation is a regulatory switch, modulating association of DCX with microtubules and actin filaments

Maryam Moslehi[1], Dominic C.H. Ng[2], and Marie A. Bogoyevitch[1*]

[1]Department of Biochemistry and Molecular Biology, University of Melbourne, Parkville, Victoria 3010, Australia

[2]School of Biomedical Sciences, University of Queensland; St Lucia, Queensland 4072, Australia
[*]marieb@unimelb.edu.au

ABSTRACT

Doublecortin X (DCX) plays essential roles in neuronal development via its regulation of cytoskeleton dynamics. This is mediated through direct interactions between its doublecortin (DC) domains (DC1 and DC2) with microtubules (MTs) and indirect association with actin filaments (F-ACT). Whilst the regulatory role of the DCX C-terminus following DC2 (i.e. DCX residues 275-366) has been established, less is known of the possible contributions made by the DCX N-terminus preceding DC1 (i.e. DCX residues 1-44). Here, we assessed the influence of DCX Ser28 within the DCX N-terminus, on the association of DCX with MTs and F-ACT. We compared the cytoskeletal interactions of the DCX S28E phosphomimetic and DCX S28A phospho-resistant mutants and wild-type DCX. Immunoprecipitation and colocalisation analyses indicated increased association of DCX S28E with F-ACT but decreased interaction with MTs, and conversely enhanced DCX S28A association with MTs but decreased association with F-ACT. To evaluate the impact of DCX mutants on cytoskeletal filaments we performed fluorescence recovery after photobleaching (FRAP) studies on SiR-tubulin and β-actin-mCherry and observed comparable tubulin and actin exchange rates in the presence of DCX WT and DCX S28A. However, we observed faster tubulin exchange rates but slower actin exchange rates in the presence of DCX S28E. Moreover, DCX S28E enhanced the association with the actin-binding protein spinophilin (Spn) suggesting the shift to favour association with both F-ACT and Spn in the presence of DCX S28E. Taken together, our results highlight a new role for DCX S28 as a regulatory switch for cytoskeletal organisation.

Keywords: Doublecortin; phosphorylation; cytoskeleton; fluorescence recovery after photobleaching

Introduction

In neuronal development, a coordinated and dynamic remodelling of the cytoskeleton is controlled by a number of filamentous actin (F-ACT)- and microtubule (MT)-regulatory proteins [1-3]. These proteins mediate cytoskeletal changes that are critical in the formation and development of axons and dendrites, the two functionally and structurally distinct extensions from the neuronal cell body that are essential for appropriate inter-neuronal communication in the nervous system [4-6]. Of these regulatory proteins, DCX can coordinate regulation of the different filament systems via its direct interactions with MTs and its indirect association with F-ACT [7, 8].

The domain organisation of the 366 amino acid DCX protein is well-characterized. Structurally, the DCX protein consists of two homologous doublecortin (DC) domains, DC1 (the N-terminal DC domain, residues 45-150) and DC2 (the C-terminal DC domain, residues 170-275) that are defining

features of the larger DCX family of proteins [9]. These DC domains are linked in tandem via a flexible unstructured region (linker) and additionally flanked by a likely unstructured N-terminal region (DCX-N, i.e. residues 1-44) and serine/proline-rich C-terminal region (DCX-C, i.e. residues 275-366) [9, 10]. The structured DC domains interact with MTs, specifically via binding to four neighboring tubulin dimers [11]. Multiple DCX mutations, causing neurodevelopmental diseases including lissencephaly, have been mapped to the DC domains. The observed defects in cortical layering arising from DCX mutations emphasize the involvement of DCX and its DC domain-mediated actions in normal neuronal migration [12, 13].

Whilst DC domain interaction with MTs is well established, an improved understanding of molecular function of DCX requires interrogation of the regulatory contributions made by the DCX termini, DCX-N and DCX-C. Importantly, DCX functions can be potentially regulated by phosphorylation of these termini by multiple different Ser/Thr kinases. Specifically, multiple sites within DCX-C including DCX Ser297 and Ser334 are phosphorylated by protein kinases cyclin-dependent kinase 5 (Cdk5) and c-Jun N-terminal kinase (JNK), respectively [14-18]. Phosphorylation of these sites decreases the affinity of DCX for MTs, to significantly impact neuronal migration [14, 19], However, protein kinases target sites in other regions of the DCX protein and the function of these phosphorylation events are less well known. Protein kinase A (PKA)-induced phosphorylation of DCX Ser47, a residue at the N-terminal extreme of the DC1 domain, can increase DCX-F-ACT association [20], raising the possibility that a translocation of DCX from MTs to ACT in a phospho-regulated fashion can influence on DCX's cytoskeletal impact. That DCX can influence F-ACT is further supported by the characterisation of an adaptor protein spinophilin (Spn). Spn, which contains multiple protein interaction domains including an ACT-binding domain and an DCX-binding domain, can act as a platform facilitating the association of ACT with the DC2 domain and DCX-C [8, 21]. Increased association of a DCX Ser47 phosphomimetic mutant with ACT in the presence of Spn reinforces a mediatory role for Spn in the DCX-ACT association however, the direct impact of DCX phosphorylation on DCX-Spn interaction remains to be investigated [21-24].

The contributions of DCX-N to the regulation of DCX actions on the cytoskeleton require further evaluation. There is one identified phosphorylation site in DCX-N, namely DCX Ser28, known to be targeted by Cdk5 but the functional consequences of phosphorylation of this residue on DCX actions in a neuronal context have not been determined [25]. The kinase activities of Cdk5 contribute to the regulation of critical cytoskeleton-dependent events including neuronal differention and neuronal plasticity via the phosphorylation of cytoskeletal regulators such as DCX, and so reinforce the importance of phosphorylation status of DCX in regulation of MT and ACT localisation in neurons during neuronal development [26].

In this study we address the modulatory role of DCX Ser28 phosphorylation on DCX interactions with MTs and F-ACT using DCX S28E and S28A mutants that mimic or prevent DCX phosphorylation respectively. Our findings from DCX co-localisation analysis with the cytoskeleton, measurements of dynamic association of DCX with MTs and F-ACT, and biochemical analyses probing the interactions of DCX with Spn reveal a critical switching mechanism involving DCX Ser28 that influences cytoskeletal organisation.

Results and Discussion

Cdk5 activity is essential for phosphorylation of DCX Ser28 and cytoskeletal organisation. Cdk5 is a member of the Cdk family of Ser/Thr kinases that, unlike other Cdk family members that are primarily involved in cell cycle control, is highly expressed in neurons and indispensable for normal brain development [26]. Cdk5 is involved in higher cognitive functions such as learning and memory formation via regulation of the cortical lamination, neuronal differentiation and synaptic plasticity [27, 28] which all rely on rapid alterations in the cytoskeleton. Genetic ablation of the *cdk5* gene results in profound remodelling of the neuronal cytoskeleton, and thus Cdk5 is regarded as an important regulatory protein for neuronal cytoskeleton dynamics through its regulation of many cytoskeleton-associated proteins [28-30].

In vitro phosphorylation and mass spectrometry studies have identified the neuronal MT-associated protein DCX as a Cdk5 substrate [15, 25]. More specifically, the DCX N-terminal site targeted by Cdk5 has been identified as DCX Ser28 [25], but the influence of DCX Ser28 phosphorylation on the neuronal cytoskeleton remains to be determined. Thus, to first establish the relationship between Cdk5 and DCX Ser28 phosphorylation in a neuronal cell context, we assessed DCX Ser28 phosphorylation status in SH-SY5Y neuroblastoma cells. Immunoblot analysis detected DCX Ser28 phosphorylation under basal culture conditions (Fig. 1A). DCX Ser28 phosphorylation levels were decreased when DCX levels were depleted by siRNA in SH-SY5Y cells (Supplementary Fig. S1A). In addition, DCX Ser28 phosphorylation was only detected in COS-1 cells transfected with wild-type (WT) DCX but not DCX Ser28 phosphomimetic and phospho-resistant mutants (supplementary Fig. S1B) confirming specificity of our antibody detection of DCX phosphorylation on Ser28. In response to Cdk5 depletion, we demonstrated a significant decrease in DCX Ser28 phosphorylation without altering total DCX levels (Fig. 1A-D). Thus, DCX Ser28 phosphorylation levels require Cdk5 in SH-SY5Y neuronal cells.

We next evaluated the impact of Cdk5 siRNA treatment on DCX Ser28 phosphorylation and the morphology of the SH-SY5Y neuroblastoma cells by immunofluorescence analysis (Fig. 1E). These studies confirmed lowered Cdk5 levels following Cdk5 siRNA transfection (Fig. 1F) accompanied by lower levels of DCX Ser28 phosphorylation (Fig. 1G). In parallel, the immunofluorescence imaging

for tubulin and F-ACT (Fig. 1H, enlarged images of regions enclosed by the white rectangles in Fig. 1E) showed cell morphology alterations that we quantitatively assessed by estimates of cell circularity. For Cdk5 siRNA-treated cells, cell circularity was significantly increased (Fig. 1I), and thus a more elongated cell shape was maintained in the presence of Cdk5.

Taken together, these results show the importance of Cdk5 as a regulator of DCX Ser28 phosphorylation and neuronal cell morphology. These observations reinforce previous studies showing that Cdk5-induced phosphorylation of DCX Ser297 that lies within the C-terminal sequence (DCX-C) could modulate association of DCX with MTs at the leading edge of the migrating neurons thus regulates neuronal migration [15]. Although DCX plays an important role in cytoskeleton organisation [29], the impact of Cdk5-induced DCX Ser28 phosphorylation on cytoskeleton organisation remains undetermined. Thus, we generated DCX Ser28 phospho-mutants, DCX S28A and DCX S28E, and assessed their association with the cytoskeleton and their influence on cytoskeleton organisation and so provide further evidence supporting a possible role in neuronal migration and movement.

DCX S28A and DCX S28E mutants define a regulated reciprocal association of DCX with MTs and F-ACT. Cdk5 decreases the affinity of DCX for MTs through its direct phosphorylation of DCX Ser297 within DCX-C [15], however the impact on cytoskeleton organization of the Cdk5-targeted phosphorylation of DCX Ser28 within DCX-N has not been previously addressed. Thus, we next used Co-IP and live imaging approaches to study the modulatory role of DCX Ser28 on DCX association with MTs and F-ACT.

SH-SY5Y cells were transfected with GFP-tagged DCX full-length (DCX WT) as a control, alongside DCX S28A (non-phospho) and DCX S28E (phospho-mimetic) mutants. Interaction of DCX proteins with MTs and F-ACT was analysed by co-immunoprecipitation using GFP-trap beads to mediate capture of GFP-DCX proteins in the pellet (bound) fraction followed by the detection of the associated α-tubulin or β-actin in each pellet fraction (Fig. 2Ai, panels as indicated). The absence of GFP-DCX proteins in supernatant (unbound) fraction (Fig. 2Aii lower panel) confirmed the complete capture of DCX proteins by the GFP-trap beads in pellet fraction (Fig. 2Ai lower panel). When compared with DCX WT, DCX S28A captured more α-tubulin while DCX S28E captured less α-tubulin (Fig. 2Ai & Fig. 2B); conversely, more β-actin was captured with DCX-S28E and less with DCX-S28A in the GFP-trap pulldown experiments (Fig. 2Ai & Fig. 2C). This suggests that DCX Ser28 phosphorylation can negatively regulate interactions with MTs. Interestingly, the inverse relationship is apparent for DCX interactions with actin.

To reinforce this role of DCX Ser28 to modulate DCX interactions with the cytoskeleton, we next extended our analyses to include colocalization imaging studies by labelling MTs (Fig. 2D & E) and F-ACT (Fig. 2F & G) with SiR-tubulin and LifeAct-mCherry labelling, repectively; enlarged images of

the regions enclosed by the white rectangles are presented also in Fig. 2D and F. Pearson correlation analysis of the live images obtained for the GFP-tagged DCX constructs revealed an increased colocalisation of DCX S28A with MTs (Fig. 2E). Conversely, DCX S28E colocalization with MTs was decreased (Fig. 2E). We observed the inverse relationship with F-actin colocalization with DCX which was decreased with DCX S28A but enhanced with DCX S28E (Fig. 2G).

Our findings therefore indicate that the DCX S28E phosphomimetic mutant can decrease the interaction with MTs. This is similar to the identified phosphoregulatory role of the DCX-C sites, Ser297 and Ser334, that are phosphorylated by the kinases Cdk5 and JNK, respectively, and that can also negatively regulate association of DCX with MTs by decreasing the affinity of interaction of DCX with MTs [19]. Indeed, the observation of increased localisation of phosphorylated DCX, together with the kinases JNK and Cdk5, at sites of neurite outgrowth emphasize the strict spatial control of DCX protein phosphorylation and its importance during neuronal migration [15, 18, 19]. Moreover, we observed the increased association of DCX S28E phosphomimetic mutant with F-ACT. This is similar to a previously identified regulatory role of PKA-induced phosphorylation of DCX Ser47 within DC1 on the DCX-ACT association and cytoskeleton organisation; a DCX Ser47 phosphomimetic mutant showed increased association with ACT but decreased interaction with MTs [20]. With our demonstration that the DCX Ser28 mutants influence the association with MTs and F-ACT, we propose DCX Ser28 as an important regulatory site within DCX-N.

To extend our observations, we next considered the possible mechanisms underlying how DCX interaction with F-ACT could be favoured. Previous imaging and co-immunoprecipitation analyses indicated that DCX directly associates with spinophilin (Spn, also known as neurabin II), an actin-binding protein critical for normal brain development [21, 22]. A coordinated function of DCX and Spn in brain development and F-ACT organisation has been supported by observations of similar phenotypic changes (hippocampal delamination and F-ACT dysregulation) in Spn-knockout or DCX-knockout mice [31]. Because Spn, via its actions as a DCX binding partner, can bind ACT and enhance ACT bundling, it can mediate the influence of DCX on ACT [31, 32]; our analyses thus far revealed the importance of DCX Ser28 in altering the association of DCX with F-ACT (i.e. an increased association of DCX S28E with ACT), and thus we next investigated the impact of DCX Ser28 phosphorylation on interaction with Spn by assessing the association of DCX S28E and DCX S28A with Spn.

The DCX S28E mutant favours association with the adaptor protein Spn. Spn is a neuronal adaptor protein that contains interaction domains for both F-ACT and DCX [21]. We therefore performed co-immunoprecipitation analysis and fixed-cell imaging to explore the association of DCX Ser28 mutants with Spn. For this analysis we chose to transfect COS-1 cells, due to their lack of endogenous DCX or Spn expression that could interfere in analysis and interpretation. We

transfected these cells with GFP-tagged DCX WT, DCX S28A or DCX S28E mutants and HA-Spn. Interaction of DCX proteins with F-ACT or HA-Spn was assessed by co-immunoprecipitation using GFP-trap beads to mediate capture of GFP-DCX proteins in the pellet (bound) fraction followed by the detection of the associated β-actin or HA-Spn in each pellet fraction (Fig. 3Ai, panels as indicated). The absence of GFP-DCX proteins in supernatant (unbound) fraction (Fig. 3Aii lower panel) again confirmed the complete capture of DCX proteins by the GFP-trap beads in pellet fraction (Fig. 3Ai lower panel). When compared to DCX WT, more β-actin and HA-Spn were captured with DCX S28E whereas less β-actin and Spn were captured with DCX S28A (Fig. 3B & Fig. 3C, respectively). Although previous studies have indicated a DCX-Spn association, this is the first study to reveal an enhanced association of Spn with a DCX phosphomimetic mutant. Because the interactions of Spn and β-actin were enhanced with the phospho-mimetic change to DCX Ser28, we propose that phosphorylated DCX Ser28 can increase F-ACT association via favouring association with Spn.

To compare the spatial relationships between DCX, Spn and F-ACT in a cellular context, we next extended our analyses to imaging of COS-1 cells co-transfected with GFP-DCX proteins and HA-Spn, with phallodin staining to visualise F-ACT (Fig. 3D, enlarged images represent regions enclosed by the white rectangles). Merge images of the panels for Spn and DCX proteins (Fig. 3 Ei, enlarged images represent regions enclosed by the white rectangles) and F-actin and DCX proteins (Fig. 3Eii, enlarged images represent regions enclosed by the white rectangles) are shown. Pearson correlation analysis of the fixed-cell images obtained for the GFP-tagged DCX proteins in association with HA-Spn or F-ACT revealed increased colocalisation of DCX S28E with Spn and F-ACT (Fig. 2Fi & ii, respectively). Thus, we observe an enhanced association of DCX S28E with Spn and F-ACT and, conversely, the decreased association of DCX S28A with Spn and F-ACT.

Taken together, these findings highlight a critical importance of DCX Ser28 as a regulatory switch that modulates association of DCX with MTs directly and with F-ACT, likely indirectly via altered interactions with the neuronal adaptor protein Spn. The increased association of DCX S28E with Spn as well as ACT highlights the role of Spn in association of phosphorylated DCX with ACT. Although previous studies indicated the increased association of DCX phosphomimetic (DCX S47E) with ACT [21], our study for the first time shows the direct impact of DCX phosphomimetic (DCX S28E) on Spn. As the dynamics of these cytoskeletal structures are regarded as critical in physiological processes including neuronal development, differentiation and movement [3], we next evaluated how DCX Ser28 may influence cytoskeleton dynamics as well as the dynamics of DCX associations with MTs and F-ACT.

Exchange rates of α-tubulin within MTs are accelerated in the presence of DCX S28E but slowed in the presence of DCX S28A. We previously reported that the association of DCX WT

with MTs slows the rate of tubulin exchange within the MT network [33]. 2-colour fluorescence recovery after photobleaching (FRAP) analyses have been instrumental for concomitant recording of the kinetics of two proteins in the same cell area e.g. cytoskeleton components and their binding proteins or two components of the same protein complex [34-36]. We therefore performed 2-colour FRAP analyses to assess firstly the impact of DCX S28A or DCX S28E mutants on MT dynamics. We monitored the dynamic recovery of two spectrally distinct fluorescently tagged proteins simultaneously in the same intracellular locale and under identical experimental conditions. Thus, in these analyses, the rates of fluorescence recovery for these proteins in a defined photobleached zone were used to quantitate rates of movement of neighbouring fluorescent molecules into the photobleached area whereas quantitative estimates of the extent of fluorescence recovery were used to estimate the exchangeable pool.

First, we assessed the influence of DCX proteins on MT dynamics (Fig. 4A, merge panels as indicated). We monitored the progress of fluorescence recovery of SiR-tubulin (Fig. 4B & C) alongside the recoveries of the transfected GFP-DCX proteins: GFP-vector (control), GFP-DCX wild-type (WT), GFP-DCX S28A or GFP-DCX S28E proteins as indicated (supplementary Fig. S2A). The progress of fluorescence recovery for each channel (green: GFP-tagged DCX proteins; red: SiR-tubulin) is further illustrated in the zoom of each photobleached area (supplementary Fig. S3A &B, respectively). We confirmed the quantitative analysis of fluorescence recovery data in Figure 4C by evaluating residuals plots (supplementary Fig. S4 Ai-iv). Furthermore, no significant impact of SiR-tubulin on MT dynamics in the presence of DCX proteins was also confirmed by the FRAP analysis of SH-SY5Y cells co-transfected with GFP-tagged α-tubulin and Myc-DCX proteins (Fig. 5, residuals analysis of fluorescence recovery data is shown in supplementary Fig. S4 Bi-iv). Thus, although SiR-tubulin is a taxol derivative, siR-tubulin at the low concentrations of SiR-tubulin (100 nM) used in our studies did not interfere with MT dynamics.

Quantitative analysis of the SiR-tubulin fluorescence recovery revealed that, relative to the fractional recovery recorded for SiR-tubulin in the presence of GFP-DCX WT, a higher fractional recovery of SiR-tubulin was observed in the presence of GFP-DCX S28E or GFP-vector but a lower fractional fluorescence recovery for SiR-tubulin in the presence of DCX S28A (Fig. 4D); and compared to the long half-maximal recovery time ($t_{1/2}$) for GFP-DCX WT, the times to reach half-maximal recovery ($t_{1/2}$) were shorter for SiR-tubulin in the presence of GFP-DCX S28E or GFP-vector only but even longer times were recorded in the presence GFP-DCX S28A (Fig. 4E). A summary for the maximum recovery and half-maximal recovery time ($t_{1/2}$) values is also presented in Fig. 4F. Therefore, not only do DCX Ser28 mutants alter association with MTs but they can also modulate MT dynamics in the area of association with DCX proteins suggesting the contribution of DCX Ser28 phosphorylation in the regulation of MT dynamics.

DCX S28A and DCX S28E mutants show opposite changes in dynamics of association with MTs. To gain additional insights into the dynamic association of DCX, and the DCX S28 mutants, with MTs, we simultaneously monitored the fluorescence recovery of the GFP-tagged DCX proteins associated with SiR-tubulin in our 2-colour FRAP analyses, (supplementary Fig. S2A & B). Quantitative analysis of these MT-associated GFP-tagged DCX proteins showed near-complete fluorescence recovery of GFP-DCX WT, comparable fluorescence recovery of GFP-DCX S28E or GFP alone but a lower fractional recovery of GFP-DCX S28A (supplementary Fig. S2C). Moreover, compared to DCX WT, the longest time to reach the half-maximal recovery ($t_{1/2}$) corresponds to DCX S28A whereas DCX S28E and GFP alone showed faster times to reach the half-maximal recovery (supplementary Fig. S2D). A summary for the maximum recovery and half-maximal recovery time ($t_{1/2}$) values is also presented in Fig. S2E. These quantitative analyses define a slower dynamic association of the DCX S28A mutant with MTs, but faster dynamic association of DCX S28E, thus revealing opposite changes in association with MTs can be modulated by DCX S28.

To further probe this relationship, and because underlying changes in MT dynamics may contribute to the observed changes in DCX dynamics, we implemented a taxol treatment strategy to stabilise MTs [30]. We observed that in the presence of taxol, MT dynamics is slower but this did not attenuate DCX protein dynamics. Indeed, analyses in taxol-treated cells showed a similar trend of fluorescence recovery as GFP-tagged DCX proteins in non-treated cells. We also confirmed the quantitative analysis of fluorescence recovery data by evaluating residuals plots (supplementary Fig. S5).; additionally, a slightly faster half-maximal recovery ($t_{1/2}$) of all DCX proteins in taxol-treated cells was observed consistently (Fig. 6). Although this may reflect an enhanced accessibility of the DCX proteins to the MT lattice in the presence of taxol, further studies are required to address the mechanisms underlying the sensing of MT changes by DCX. Importantly, our results reinforce the interpretation that the slower dynamic association of DCX S28A or faster dynamic association of DCX S28E with MTs is not dependent on the dynamics of α-tubulin exchange within the MTs themselves. These observations reveal that DCX S28E mutant increases the dynamics of association with MTs but DCX S28A has the opposite effect.

Taken together, decreased association but increased dynamics of the DCX S28E and its associated MTs have been observed. These results highlight a novel phosphoregulatory role of DCX Ser28 in the dynamics of DCX-MT association. We previously indicated the strikingly fast dynamics of DCX in association with MTs [33] proposing that DCX does not interfere with other binding proteins including motor proteins essential for protein trafficking along the MTs. Therefore, enhanced dynamics of DCX S28E association with MTs suggests that DCX Ser28 phosphorylation may regulate dynamics of MTs in association with MT-binding proteins. Building on our observations of altered F-ACT affinities for the DCX S28 mutants (Fig 2), we next evaluated the impact of DCX S28A and DCX S28E mutants on F-ACT dynamics.

Exchange rates of β-actin within F-ACT are accelerated in the presence of DCX S28A but slowed in the presence of DCX S28E. DCX knockout mice show marked actin dysregulation with impaired axon guidance and preserved axonal elongation [31]. These phenotypes are similar to the phenotypes observed in animal models with targeted deletion of actin-regulatory proteins emphasizing an important role for DCX in actin regulation and organisation [31, 32]. Our observations of a reciprocal association of DCX S28A and DCX S28E mutants with F-ACT (Fig. 2), as well as the modulation of MT and DCX protein dynamics, prompted our analysis of the impact of DCX S28A or S28E mutants on β-actin dynamics.

We applied 2-colour FRAP analyses (Fig. 7A, merge panels as indicated) and monitored fluorescence recovery of β-actin-mCherry (Fig 7B & C) alongside the recoveries of the transfected GFP-DCX proteins: GFP-vector (control), GFP-DCX wild-type (WT), GFP-DCX S28A or GFP-DCX S28E proteins as indicated (supplementary Fig. S6). The progress of fluorescence recovery for each channel (green: GFP-tagged DCX proteins; red: β-actin-mCherry) is further illustrated in the zoom of each photobleached area (supplementary Fig. S7A &B, respectively). Again we confirmed the quantitative analysis of fluorescence recovery data in Figure 7C by evaluating residuals plots (Fig. S4 Ci-iv).

Quantitative analysis of the β-actin-mCherry fluorescence recovery revealed, relative to the fractional recovery recorded in the presence of GFP-DCX WT, a comparable fractional recovery in the presence of GFP-DCX S28A or GFP-vector, but a lower fractional fluorescence recovery in the presence of DCX S28E (Fig. 7D); compared to the half-maximal recovery time ($t_{1/2}$) for GFP-DCX WT. The times to reach half-maximal recovery ($t_{1/2}$) were shorter for β-actin-mCherry in the presence of GFP-DCX S28A or GFP-vector only but longer time was recorded in the presence GFP-DCX S28E (Fig. 7E). A summary of the maximum recovery and $t_{1/2}$ values is also presented in Fig. 7F. Thus, these results reveal the additional impact of DCX Ser28 to regulate the dynamics of DCX association with F-ACT, and thus the potential for DCX Ser28 phosphorylation to modulated actin-based functions in axonal elongation processes in neuronal migration [31, 32].

Taken together, our studies reveal the importance of the only identified phosphorylation target for Cdk5 within DCX-N, DCX Ser28, as regulatory switch modulating association of DCX with MTs and F-ACT; this parallels the previous findings on the impact of DCX Ser47 phosphorylation in modulation of interaction with MTs and F-ACT [20] and further emphasizes an adaptor role for interaction of DCX with Spn [21-24]. This is the first study to show the influence of DCX Ser28 phosphorylation on interaction with Spn which further explains the modulatory role of DCX Ser28 in ACT localisation and organisation. These findings highlight the critical regulatory roles that the DCX non-structured sequences outside the DC-domains will play in defining DCX actions. We previously proposed that phosphorylation of DCX in these non-structured sequences could influence DCX

association dynamics with MTs [33] and here we propose that DCX Ser28 phosphorylation also might modulate the dynamics of DCX with MTs and F-ACT suggesting the importance of DCX Ser28 phosphorylation in regulation of transition between MTs and F-ACT by modulation of DCX association and dynamics of association. Since neuronal migration involves formation and disruption of MT and ACT structures at the leading edge of the migrating neurons, cytoskeleton-associated proteins such as DCX will play critical roles [1, 3]. Based on our findings, we suggest that DCX Ser28 phosphorylation regulates appropriate neuronal migration by acting as a regulatory switch to facilitate the regulation of MTs and F-ACT growth and disruption in migrating neurons during brain development.

In future studies, we propose that it will be critical to address the contributions of other DCX phosphorylation sites in modulating DCX association with the cytoskeleton to investigate the coordinated or similar impacts of DCX phosphorylation sites on MT and ACT dynamics. Moreover, DCX structural studies should be the priority for future exploration as phosphorylation of DCX termini might lead to allosteric modulation of DCX itself or alter its association with DCX binding partners.

Methods

Mammalian expression plasmids

Wildtype (WT) GFP-DCX and Myc-DCX WT constructs were made as previously described [33]. The GFP-DCX S28A, GFP–DCX S28E, myc-DCX S28A and myc-DCX S28E mutants were generated by site-directed mutagenesis followed by DpnI digestion. The PCR primer pairs are listed in Supplementary Table S1. All constructs were validated by restriction digestion and full sequence analysis. The plasmid expressing GFP-α-tubulin and GFP-β-actin plasmids were provided by Patricia Wadsworth (Addgene plasmid #12298) and Ryohei Yasuda (Addgene plasmid #21948), respectively. The β-actin-mCherry plasmid was a gift from Dr. Elizabeth Hinde (University of Melbourne, Australia) and the HA-spinophilin (neurabin II) plasmid was a gift from Professor Tetsu Akiyama (University of Tokyo, Japan).

Cell culture, transfection and treatments

Analyses were performed in human neuroblastoma SH-SY5Y cells and monkey fibroblastoma COS-1 cells that were maintained (37 ℃, 5% CO_2) in growth media (for COS-1 cells, high-glucose Dulbecco's modified Eagle's medium (DMEM) and for SH-SY5Y cells, high-glucose Dulbecco's modified Eagle's medium/F-12 (DMEM/F-12)) containing L-glutamine supplemented with 10% (v/v) fetal bovine serum (FBS), 1mM penicillin and streptomycin. For MT stabilization, cells were treated with taxol (10 μM, 1h; Sigma) prior to analysis. For assessment of DCX actions, transient

transfections were performed using Lipofectamine™ 2000 and serum-free Opti-MEM medium according to the manufacturer's instructions (Invitrogen).

siRNA transfection

Cdk5 (L-003239-00-0005) or DCX (L-011113-00-0005) as well as control siRNA (D-001810-01-05) were designed and synthesized by Dharmacon. SH-SY5Y cells were transfected with these siRNAs using DharmaFECT transfection reagent according to the manufacturer's instructions (Dharmacon). Briefly, cells were seeded in a 6-well plate at a confluence of 60-70%. 10 µl of siRNA (5 µM) and 10 µl of DharmaFECT transfection reagent were diluted in serum-free OPTI-MEM medium separately (total volume: 200 µl) and incubated at room temperature for 5 min. Then tubes were mixed and incubated for further 20 min to form a complex. Cells were washed and incubated with the antibiotic-free DMEM/F12 (1.6 ml) and the siRNA complex were added to cells to reach the total transfection volume of 2 ml. Cells were incubated (37℃ in 5% CO_2) for 48 h for immunofluorescence microscopy and 72 h for immunoblot analysis.

Cell lysis, immunoblotting and co-immunoprecipitation

Cell lysates were prepared using RIPA buffer [50 mM Tris-HCl, pH 7.3, 150 mM NaCl, 0.1 mM ethylenediaminetetraacetic acid (EDTA), 1% (w/v) sodium deoxycholate, 1% (v/v) Triton X-100, 0.2% (w/v) NaF and 100 µM Na_3VO_4] supplemented with complete protease inhibitor mix (Roche Diagnostic 4693159001). Cell lysates were incubated on ice (10 min) and cleared by centrifugation (16,000 g, 10 min). Protein concentrations were determined by the Bradford protein assay.

For immunoblot analysis, protein samples diluted with 3X protein sample buffer were resolved by SDS-PAGE [10% (v/v) polyacrylamide gels] and the separated proteins were transferred onto polyvinylidene difluoride (PVDF) membranes (EMD Millipore). Proteins of interest were detected using the following primary antibodies: anti-DCX (ThermoFisher 48-1200), anti-DCX pSer28 (Abcam 23544), anti-Cdk5 (Santa Cruz Biotechnology sc-249), anti-spinophilin (EMD Millipore 06-852), anti-GFP (Abcam 13970), anti-β-actin (Sigma A5441) and anti-α-tubulin (Sigma T6074). After incubation with horseradish peroxidase-linked secondary antibodies (Thermo Scientific), immunoreactive proteins were visualized using an enhanced chemiluminescence detection system (Thermo Scientific) and quantitation carried out using FIJI 2.0 public domain software (National Institutes of Health).

Co-immunoprecipitations to assess DCX interactions with MTs, actin or Spn were performed by incubating protein lysates (2 mg) with GFP-trap beads (ChromoTek; room temperature, 1 h). The supernatant was removed following centrifugation (16,000 g, 30 s) and the beads were thoroughly washed (3x washing with 0.5 ml lysis buffer) before associated proteins were eluted by the addition

of 3X protein sample buffer and boiling (100℃, 5 min). Precipitated protein and supernatants were resolved by SDS-PAGE and immunoblotted as described above.

Immunofluorescence imaging

Cells were cultured on uncoated glass coverslips, then washed in PBS before fixing with 4% (w/v) paraformaldehyde (20 min, room temperature). Cells were then permeabilised with 0.2% (w/v) Triton X-100 in PBS and blocked with 10% (v/v) fetal calf serum, before incubation with the following primary antibodies diluted in 1% (w/v) BSA in PBS: anti-α-tubulin (Abcam 18251), anti-DCXpSer28 (Abcam 23544), anti-HA tag (Thermo Scientific 26183), anti-Cdk5 (Santa Cruz Biotechnology sc-249) and anti-Spinophilin (EMD Millipore 06-852) where indicated and Alexa Fluor conjugated secondary antibodies diluted in 1% (w/v) BSA in PBS for 1 h each. Also, to detect actin filaments, cells were incubated with Alexa Fluor 568 phalloidin (Thermo Scientific A12380) for 1 h prior to mounting on coverslips. Coverslips were mounted with Vectashield reagent (Vector Laboratories) and images were acquired on a ZEISS LSM 800 confocal laser scanning microscope equipped with a 63x 1.4 NA objective (Biological Optical Microscopy Platform, University of Melbourne).

Live-cell imaging microscopy

SH-SY5Y cells were seeded on eight-well µ-slides (Ibidi) and transiently transfected with plasmids encoding GFP-DCX constructs alone or co-transfected with β-actin-mCherry (Addgene). At 24 h post-transfection, the culture medium was replaced with fresh medium containing 100 nM MT probe SiR-tubulin dye (Cytoskeleton Inc. CY-SC002) [38] where indicated. After additional incubation (12 h) with the SiR-tubulin dye, the culture medium was replaced with pre-warmed Phenol-Red-free DMEM growth medium. To confirm the results obtained with β-actin-mCherry plasmid transfection or analysis of cells stained with the SiR-tubulin dye, cells were also co-transfected to express GFP-β-actin with myc-DCX constructs or to co-express GFP-α-tubulin with myc-DCX constructs. Images were captured on a Leica TCS SP5 confocal microscope equipped with an environmental chamber (37 ℃, 5% CO_2) using a 63X 1.4 NA objective (Biological Optical Microscopy Platform, University of Melbourne). Live-cell images (n= 40 random cells per DCX protein) were captured to analyze the correlation of the localization of the GFP-DCX proteins with MTs or F-ACT.

Quantitative imaging analysis

SH-SY5Y cells were analyzed for the degree of correlation of localization between fluorophores and the Pearson correlation coefficient was calculated using the JaCoP plugin in FIJI software. A higher Pearson correlation coefficient corresponds to greater colocalisation of two fluorophores [37]. SH-SY5Y cells were analyzed for cell shape circularity using FIJI (ImageJ) software. After the quantiation of each cell's area and perimeter, the circularity value was calculated as: $4\pi \times$

([*Area*]/[*Perimeter*]^2); resulting values of circularity thus range from 0 (equivalent to an infinitely elongated cell) to 1 (equivalent to a perfect circle).

Fluorescence recovery after photobleaching (FRAP)

Photobleach analyses were performed with cells maintained in Phenol-Red-free growth medium prior to imaging at 37 ℃ with 5% CO_2 supplied to the microscope chamber. Images were captured on a Leica TCS SP5 confocal microscope equipped with an environmental chamber (37 ℃, 5% CO_2) using a 63X 1.4 NA objective (Biological Optical Microscopy Platform, University of Melbourne). The settings for scanning were as follows: bidirectional scanning at 400 Hz, 20% laser power at 488 nm for GFP-DCX constructs and 594nm for LifeAct-mCherry or 633 nm for SiR-tubulin. Fluorescence emissions from EGFP and mCherry or SiR-tubulin dye were detected simultaneously in two channels. Bleaching for ten images was performed with a single pass with all laser lines between 488 nm and 594 nm or 633 nm set to maximal power. A region of interest (ROI) was set as a square (4 μm^2) and the average frame rates were 1 frame/64ms. Fluorescence recovery was recorded at 0.6-s intervals for 60 s and representative images were shown for 3, 6, 9, 30 and 60 s post-bleaching. FRAP measurements (n = 10 random cells) were normalized as described previously [34-36]:

$F_{frap\text{-}norm(t)} = (F_{whole\text{-}prebleach}/[F_{whole(t)}\text{-}F_{bg(t)}])(F_{frap(t)}\text{-}F_{bg(t)}/F_{frap\text{-}prebleach})$,

Where $F_{frap(t)}$ is the fluorescence recovery in the photobleached ROI at time *t,* $F_{whole(t)}$ is the whole-cell fluorescence and $F_{bg(t)}$ is the background region fluorescence intensity (outside the cell). $F_{frap\text{-}prebleach}$ and $F_{whole\text{-}prebleach}$ represent mean prebleach fluorescence intensity of the photobleached ROI and the whole cell, respectively.

Normalised FRAP measurements were plotted against postbleach recovery time and the resulting data fitted with either the single [$F_{(t)}=A(1\text{-}exp^{-\tau.t})$] or double exponential equation [$F_{(t)}=A_1(1\text{-}exp^{-\tau 1.t}) + A_2(1\text{-}exp^{-\tau 2.t})$].

Data fitted single exponential equation indicates one phase association as A represents the fluorescence recovery plateau and the time to reach half-maximal recovery ($t_{1/2}$) is calculated as $t_{1/2} = \ln(2)/\tau$.

Alternatively, data fitted with double exponential equation illustrate two phase (fast and slow phases) association as A_1 = (Plateau)(Percent of the signal in the fast phase)0.1, A_2 = (Plateau)(100-Percent of the signal in the fast phase)0.1 and $t_{1/2}$ for the fast and slow phases are calculated using τ_1 and τ_2, respectively.

In our study, all FRAP data were fitted to single exponential equation representing one phase association.

Statistical analysis

Statistical analyses of data sets for deviation from a normal distribution were carried out with GRAPHPAD PRISM 6 software using the D'Agostino-Pearson omnibus normality test. Data sets with normal distribution were analyzed using unpaired two-tailed student's *t*-test analyses of differences between the control and test conditions (* $p \leq 0.05$, ** $p \leq 0.01$, *** $p \leq 0.001$, **** $p \leq 0.0001$) whereas data sets with deviation from normal distribution were analyzed using Mann-Whitney and Kruskal-Wallis non-parametric test ($^{\#}p \leq 0.05$, $^{\#\#}p \leq 0.01$, $^{\#\#\#}p \leq 0.001$, $^{\#\#\#\#}p \leq 0.0001$) as indicated.

References

1. Takano, T., Xu, C., Funahashi, Y., Namba, T. & Kaibuchi, K. Neuronal polarization. *Development*. 142(12), 2088-2093 (2015).

2. Witte, H. & Bradke, F. The role of the cytoskeleton during neuronal polarization. *Curr Opin Neurobiol*. 18 (5), 479-487 (2008).

3. Hur, E. M., Saijilafu & Zhou, F. Q. Growing the growth cone: remodeling the cytoskeleton to promote axon generation. *Trends Neurosci*. 35(3), 164-174 (2012).

4. Geraldo, S. & Gordon-Weeks, P. R. Cytoskeletal dunamics in growth-cone steering. *J Cell Sci*. 122(Pt 20), 3595-3604 (2009).

5. Baas, P. W., Lin, S. H. The story of microtubule polarity orientation in the neuron. *Dev Neurobiol*. 71(6), 403-418 (2011).

6. Hoogenraad, C. C. & Bradke, F. Control of neuronal polarity and plasticity-a renaissance for microtubules?. *Trends Cell Biol*. 19, 669-676 (2009).

7. Rodriguez, O. C., Schaefer, A. W., Mandato, C. A., Forscher, P., Bement, W. M. & Waterman-Storer, C. M. Conserved microtubule-actin interactions in cell movement and morphogenesis. *Nat Cell Biol*. 5, 599-609 (2003).

8. Tsukuda, M., Prokscha, A., Ungewickell, E., Eichele, G. Doublecortin association with actin filaments is regulated by Neurabin 2. *J Biol Chem*. 280, 11361-11368 (2005).

9. Fourniol, F., Perderiset, M., Houdusse, A. & Moores, C. Structural studies of the doublecortin family of MAPs. *Methods. Cell. Biol.* 115, 27-48 (2013).

10. Kim, M. H., Cierpicki, T., Derewenda, U., Krowarsch, D., Feng, Y., Devedjiev, Y., Dauter, Z., Walsh, C. A., Otlewski, J., Bushweller, J. H. & Derewenda, Z. S. The DCX-domain tandems of doublecortin and doublecortin-like kinase. *Nat. Struct. Biol.* 10, 324-333 (2003).

11. Fourniol, F.J., Sundelar, C. V., Amigues, B., Clare, D. K., Thomas, G., Perderiset, M., Francis, F., Houdusse, A. & Moores, C. Template-free 13-protofilament microtubule-MAP assembly visualized at 8 A resolution. *J. Cell. Biol.* 191, 463-470 (2010).

12. Des Portes, V., Pinard, J. M., Billuart, P., Vinet, M. C., Koulakoff, A., Gelot, A., Dupuis, E., Motte, J., Berwald-Netter, Y., Catala, M., Kahn, M., Beldjord, C. & Chelly, J. A novel CNS gene required for neuronal migration and involved in X-linked subcortical laminar heterotopia and lissencephaly syndrome. *Cell*. 92, 51-61 (1998).

13. Gleeson, J. G., Allen, K. M., Fox, J. W., Lamperti, E. D., Berkovic, S., Scheffer, I., Cooper, E. C., Dobyns, W. B., Minnerath, S. R., Ross, M. E. & Walsh, C. A. Doublecortin, a brain-specific gene mutated in human X-linked lissencephaly and double cortex syndrome, encodes a putative signaling protein. *Cell.* 92, 63-72 (1998).

14. Schaar, B. T., Kinoshita, K. & McConnell, S. K. Doublecortin microtubule affinity is regulated by a balance

of kinase and phosphatase activity at the leading edge of migrating neurons. *Neuron*. 41, 203-213 (2004).

15. Tanaka, T., Serneo, F. F., Tseng, H., Kulkarni, A. B., Tsai, L. & Gleeson, J. G. Cdk5 phosphorylation of doublecortin Ser297 regulates its effect on neuronal migration. *Neuron*. 41, 215-227 (2004).

16. Gdalyahu, A., Ghosh, I., Levy, T., Sapir, T., Sapoznik, S., Fishler, Y., Azoulai, D. & Reiner, O. DCX, a new mediator of the JNK pathway. *EMBO J.* 23, 823-832 (2004).

17. Reiner, O., Gdalyahu, A., Ghosh, I., Levy, T., Sapoznik, S., Nir, R. & Sapir, T. DCX's phosphorylation by not just another kinase (JNK). *Cell Cycle* 3, 747-751 (2004).

18. Jin, J., Suzuki, H., Hirai, S., Mikoshiba, K. & Ohshima, T. JNK phosphorylates Ser332 of doublecortin and regulates its function in neurite extension and neuronal migration. *Dev. Neurobiol*. 70(14), 929-942 (2010).

19. Ramkumar, A., Jong, B. Y. & Ori-McKenney, K. M. ReMAPping the microtubule landscape: How phosphorylation dictates the activities od microtubule-associated proteins. Dev. Dyn247(1). 138-155 (2018). Doi: 10.1002/dvdy.24599

20. Toriyama, M., Mizuno, N., Fukami, T., Iguchi, T., Toriyama, M., Tago, K. & Itoh, H. Phosphorylation of doublecortin by protein kinase A orchestrates microtubule and actin dynamics to promote neuronal progenitor cell migration. *J. Biol. Chem*. 287(16), 12691-12702 (2012).

21. Tsukuda, M., Prokscha, A., Oldekamp, J., Eichele, G. Identification of Neurabin 2 as a novel doublecortin interacting protein. *Mech. Dev*. 120, 1033-1043 (2003).

22. Satoh, A., Nakanishi, H., Obaishi, H., Wada, M., Takahashi, K., Satoh, K., Hirao, K., Nishioka, H., Hata, Y., Mizoguchi, A. & Takai, Y. Neurabin II/Spinophilin. *J. Biol. Chem*. 273, 3470-3475 (1998).

23. Allen, P. B., Ouimet, C. C. & Greengard, P. Spinophilin, a novel protein phosphatase 1 binding protein localized to dendrite spines. *Proc. Natl. Acad. Sci. USA*. 94, 9956-9961 (1997).

24. Tsukuda, M., Prokscha, A. & Eichele, G. Neurabin II mediates doublecortin-dephosphorylation on actin filaments. *Biochem Biophys Res Commun*. 343, 839-847 (2006).

25. Graham, M. E., Ruma-Haynes, P., Capes-Davis, A. G., Dunn, J. M., Tan, T. C., Valova, V. A., Robinson, P. J. & Jeffrey, P. L. Multisite phosphorylation of doublecortin by cyclin-dependent kinase 5. *Biochem. J*. 381(Pt 2), 471-481 (2004).

26. Nikolic, M., Dudek, H., Kwon, Y. T., Ramos, Y. F. & Tsai, L. H. The cdk5/p35 kinase is essential for neurite outgrowth during neuronal differentiation. *Genes Dev*. 10, 816-825 (1996).

27. Ohshima, T., Ward, J. M., Huh, C. G., Longenecker, G., Veeranna, Pant, H. C., Brady, R. O., Martin, L. J. & Kulkarni, A. B. Targeted disruption of the cyclin-dependent kinase 5 gene results in abnormal corticogenesis, neuronal pathology and perinatal death. *Proc. Natl. Acad. Sci. USA.* 93, 11173-11178 (1996).

28. Tanaka, T., Veeranna, Ohshima, T., Rajan, P., Amin, N. D., Cho, A., Sreenath, T., Pant, H. C., Brady, R. O. & Kulkarni, A. B. Neuronal cyclin-dependent kinase 5 activity is critical for survival. *J. Neurosci*. 21, 550-558 (2001).

29. Shah, K. & Lahiri, D. K. A tale of the Good and Bad: Remodeling of the microtubule network in the brain by Cdk5. *Mol. Neurobiol.* 54(3), 2255-2268 (2017). Doi: 10.1007/s12035-016-9792-7

30. McLinden, K. A., Trunova, S. & Giniger, E. At the fulcrum in health and disease: Cdk5 and the balancing acts of neuronal structure and physiology. *Brain Disord. Ther*. (Suppl 1), 001(2012). Doi: 10.4172/2168-975X

31. Fu, X., Brown, K. J., Yap, C. C., Winckler, B., Jaiswal, J. & Liu, J. S. Doublecortin (Dcx) family proteins regulate filamentous actin structure in developing neurons. *J. Neurosci.* 33(2), 709-721 (2013). Doi: 10.1523/JNEUROSCI.4603-12.2013.

32. Bielas, S. L., Serneo, F. F., Chechlacz, M., Deerinck, T. J., Perkins, G. A., Allen, P. B., Ellisman, M. H. & Glesson, J. G. Spinophilin facilitates dephosphorylation of doublecortin by PP1 to mediate microtubule bundling at the axonal wrist. Cell. 129(3), 579-591 (2007). Doi: 10.1016/j.cell.2007.03.023

33. Moslehi, M., Ng, D. C. H. & Bogoyevitch, M. A. Dynamic microtubule association of Doublecortin X (DCX) is regulated by its C-terminus. *Sci. Rep.* 7(1):5245 (2017). doi: 10.1038/s41598-017-05340-x.

34. Picard, D., Suslova, E. & Briand, P. A. 2-color photobleaching experiments reveal distinct intracellular dynamics of two components of the Hsp90 complex. *Exp. Cell. Res.* 312 (19), 3949-3958 (2006).

35. Breuzard, G., Hubert, P., Nouar, R., De Bessa, T., Devred, F., Barbier, P., Sturgis, J. N. & Peyrot. V.

Molecular mechanisms of Tau binding to microtubules and its role in microtubule dynamics in live cells. *J. Cell. Sci.* 126, 2810-2819 (2013).

36. Lim, N. R., Yeap, Y. Y., Zhao, T. T., Yip, Y. Y., Wong, S. C., Xu, D., Ang, C. S., Williamson, N. A., Xu, Z., Bogoyevitch, M. A. & Ng, D. C. Opposing roles for JNK and Aurora A in regulating the association of WDR62 with spindle microtubules. *J. Cell. Sci.* 128, 527-540 (2015).

37. Bolte, S. & Cordelieres, F. P. A guided tour into subcellular colocalisation analysis in light microscopy. J. Microsc. 224(Pt 3), 213-232 (2006).

38. Lukinavičius, G., Reymond, L., D'Este, E., Masharina, A., Göttfert, F., Ta, H., Güther, A., Fournier, M., Rizzo, S., Waldmann, H., Blaukopf, C., Sommer, C., Gerlich, D. W., H. D., Hell, S. W. & Johnsson, K. Fluorogenic probes for live-cell imaging of the cytoskeleton. *Nat. Methods*. 11, 731-3 (2014).

Acknowledgements

M.M. acknowledges the scholarship support by the University of Melbourne (Melbourne Research Scholarship). D.N. is supported by an ARC Future Fellowship (FT120100193). We acknowledge that all image acquisition and quantitative image analysis was performed within the Biological Optical Microscopy Platform (BOMP) of the University of Melbourne. We thank Professor Orly Reiner (Weizmann Institute of Science, Israel) for supplying the DCX full-length plasmid and we also thank professor Tetsu Akiyama (University of Tokyo, Japan) for supplying the HA-neurabin II plasmid. β-actin-mCherry is also a gift from Dr. Elizabeth Hinde (University of Melbourne).

Author contributions statement

All authors conceived the experiments and experimental design. M.M. conducted all experiments, analysed the results and drafted the manuscript. All authors reviewed the manuscript.

Competing financial interests

The authors declare no competing financial interests.

Figure Legends

Figure 1. Cyclin-dependent kinase 5 (cdk5) regulates DCX Ser28 phosphorylation and cell morphology. (A-E) SH-SY5Y cells were transfected with negative control siRNA or cdk5 siRNA in order to study the impact of cdk5 on DCX Ser28 phosphorylation and cell morphology. **(A)** Following control or cdk5 siRNAs transfections, immunoblotting was performed using antibodies against cdk5, DCXpSer28 or DCX (panels as indicated). Equivalent protein loading was detected by immunoblotting for total α-tubulin (lower panel). For siRNA-transfected cells, cdk5, DCXpSer28 or DCX levels were measured by quantitating the **(B)** cdk5 to total α-tubulin, **(C)** DCXpSer28 to DCX or **(D)** DCX to total α-tubulin ratio. Error bars represent the standard error of the means and asterisks indicate values calculated to be statistically significantly different (**p≤0.01 n= 3 independent experiments. n.s.= not significant). **(E)** Fixed-cell imaging was conducted applying antibodies to visualise the cdk5, phosphorylated DCX Ser28, MT or applying phalloidin to visualise ACT in negative control- or cdk5 siRNA transfected cells (panels as indicated). DAPI-stained nuclei were visualised as blue in merge panels. Scale bars represent 10 µm. To measure the **(F)** cdk5 expression or **(G)** DCXpSer28 expression, the fluorescence intensity per cell area was indicated. Error bars represent the standard error of the means and asterisks indicate values calculated to be statistically significantly different (****p≤0.0001 n=40 randomly selected cells). **(H)** Enlarged images of regions enclosed by the white rectangles in Fig. E and **(I)** cell morphology of the negative control siRNA or cdk5 siRNA transfected SH-SY5Y cells was estimated by cell circularity analysis. Error bars represent the standard error of the means and asterisks indicate values calculated to be statistically significantly different (****p≤0.0001 n=40 randomly selected cells).

Figure 2. DCX S28A and DCX S28E mutants show reciprocal association with MTs and F-ACT. (A-C) Lysates prepared from SH-SY5Y cells expressing GFP-DCX WT, GFP-DCX S28A and GFP-DCX S28E were incubated with GFP-trap beads for 1h followed by centrifugation to collect the GFP-trap beads and associated GFP-tagged constructs. Immunoblotting was performed to detect the endogenous α-tubulin (upper panel) or β-actin (middle panel) in (**Ai**) pellet fraction containing precipitated GFP constructs or (**Aii**) supernatant fraction. For pellet fraction, α-tubulin or β-actin levels were measured by quantitating the **(B)** α-tubulin to GFP-tagged constructs or **(C)** β-actin to GFP-tagged constructs ratio. Error bars represent the standard error of the means and asterisks indicate values calculated to be statistically significantly different (*p≤0.05, **p≤0.01, ***p≤0.001, ****p≤0.0001 n=3 independent experiments). **(D-G)** Live imaging was conducted to evaluate cytoskeleton organisation in association with DCX proteins. Live images of the SH-SY5Y cells expressing GFP-DCX WT, GFP-DCX S28A or GFP-DCX S28E together with **(D)** SiR-tubulin probe to visualise MTs or **(F)** expression of LifeAct-mCherry to visualise F-ACT were performed. Merge images indicate the colocalisation of GFP-DCX proteins with MTs (right panels in **D**, enlarged images of regions enclosed by the white rectangles in Fig. D) or F-ACT (right panels in **F**, enlarged images of regions enclosed by the white rectangles in Fig. F). Scale bars represent 10 µm. The Pearson coefficient was measured for GFP-tagged DCX proteins and **(E)** MTs or **(G)** F-ACT to assess colocalisation where 0 indicates no correlation between two channels whereas 1 indicates complete correlation of two channels. Error bars represent the standard error of the means and asterisks indicate values calculated to be statistically significantly different (***p≤0.001, ****p≤0.0001 n=40 randomly selected cells).

Figure 3. Reciprocal association of DCX S28A and S28E mutants with Spn follows the same trend as association of DCX Ser28 mutants with F-ACT. (A-C) Lysates prepared from COS-1 cells co-expressing GFP-DCX WT, GFP-DCX S28A or GFP-DCX S28E with HA-tagged Spn were incubated with GFP-trap beads for 1h followed by centrifugation to collect the GFP-trap beads. Immunoblotting was performed to detect the endogenous β-actin (upper panel) or exogenous HA-Spn (middle panel) in the (**Ai**) pellet fraction contains GFP constructs or (**Aii**) supernatant fraction. For pellet fraction, β-actin or Spn levels were measured by quantitating the **(B)** β-actin to GFP-tagged constructs or **(C)** Spn to GFP-tagged constructs ratio. Error bars represent the standard error of the means and asterisks indicate values calculated to be statistically significantly different (*p≤0.05, **p≤0.01, ***p≤0.001, ****p≤0.0001 n=3 independent experiments). **(D & E)** Fixed-cell

imaging was conducted to evaluate the association of DCX proteins with Spn or F-ACT. **(D)** COS-1 cells co-expressing GFP-DCX WT, GFP-DCX S28A or GFP-DCX S28E (visualised as green) together with HA-Spn were fixed and Spn or F-ACT were visualised using HA tag antibody (visualised as red) or phalloidin (visualised as purple), respectively. Nuclei were stained with DAPI (visualised as blue). Merge images indicate the co-localisation of all 4 channels;Enlarged images of regions enclosed by the white rectangles in Fig. D. **(E)** Colocalisation of the **(i)** HA-Spn and GFP-DCX proteins or **(ii)** F-ACT and GFP-DCX proteins (enlarged images of regions enclosed by the white rectangles in Fig. E) were quantitated as the Pearson correlation coefficient (Fi and Fii, respectively) where 0 indicates no correlation between two channels whereas 1 indicates complete correlation of two channels. Error bars represent the standard error of the means and asterisks indicate values calculated to be statistically significantly different (**p≤0.01, ***p≤0.001, ****p≤0.0001 n=40 randomly selected cells for each GFP-DCX construct).

Figure 4. DCX S28A slows tubulin exchange rate within the MTs but DCX S28E accelerates MT dynamics. (A-C) SH-SY5Y cells were transfected with GFP-vector (control), GFP-DCX WT, GFP-DCX S28A and GFP-DCX S28E and stained with SiR-tubulin probe to visualise MTs. Dual FRAP protocol was performed to monitor the simultaneous recovery of GFP-tagged constructs and SiR-tubulin. Panels in **(A)** represents the merge images of the GFP-tagged constructs and SiR-tubulin stained MTs (panels as indicated) and panels in **(B)** indicates SiR-tubulin only. Representative images in **(A)** and **(B)** are photobleached in a small ROI indicated by the white rectangle in cell images for bleach time-point and **(C)** quantitative analysis were performed for the fluorescence recovery subsequently monitored post-bleach at 0.6 s intervals for 60 s. Images are shown at 3 s interval for 60 s. regression values (R^2) of the respective curve fits are indicated. Scale bars represent 10 µm. **(D & E)** Pooled quantitative parameters derived from dual-colour FRAP imaging data for the SiR-tubulin stained MTs in association with GFP-tagged constructs and the recovery of the ROI fluorescence for SiR-tubulin associated with GFP-DCX proteins was indicated. Results are for the mean ±SEM for **(D)** the fluorescence maximum recovery for SiR-tubulin in the bleached areas and **(E)** the time to reach the half-maximal recovery of fluorescence ($t_{1/2}$) for SiR-tubulin associated with GFP-DCX proteins. Error bars represent the standard error of the means and asterisks indicate values calculated to be statistically significantly different (*p≤0.05, ****p≤0.0001 n=10 randomly selected cells. n.s. = not significant). **(F)** FRAP data summary.

Figure 5. FRAP analysis reveals that DCX S28A slows MT dynamics while DCX S28E accelerates MT dynamics. (A & B) SH-SY5Y cells were transfected to co-express GFP-α-tubulin with myc-vector (control), myc-DCX WT, myc-DCX S28A and myc-DCX S28E. **(A)** Fluorescence recovery was subsequently monitored post-bleach at 3 s intervals for 60 s. Scale bars represent 10 µm. **(B)** Plots of the fluorescence recovery in the small area of bleach (indicated by the white rectangle) for GFP-α-tubulin are shown. Regression values (R^2) for the accuracy of each curve fit are indicated. **(C & D)** Pooled quantitative parameters derived from FRAP imaging data for the GFP-α-tubulin in association with myc-tagged constructs and the recovery of the ROI fluorescence for GFP-α-tubulin were indicated. Results are for the mean ± SEM for **(C)** the fluorescence maximum recovery for GFP-α-tubulin in the bleached area and **(D)** the time to reach half-maximal recovery of fluorescence ($t_{1/2}$). Error bars represent the standard error of the means and asterisks indicate values calculated to be statistically significantly different (*p≤0.05, **p≤0.01, ***p≤0.001, ****p≤0.0001 n=10 randomly selected cells. n.s.=not significant). **(E)** FRAP data summary.

Figure 6. FRAP analysis reveals that taxol-induced MT stabilisation does not slow the dynamics of DCX Ser28 mutants in association with MTs. (A-D) SH-SY5Y cells were transfected to express GFP-vector, GFP-tagged DCX WT, S28A or S28E co-stained with SiR-tubulin to probe MTs. Cells were incubated with taxol (10 µM, 1h) prior to the FRAP protocol. **(Ai, Bi, Ci & Di)** The fluorescence recovery of the SiR-tubulin was subsequently monitored post-bleach at 0.6 s intervals for 60 s and plots of the recovery of fluorescence in the bleach area are shown for non-treated (indicated as black curve) and taxol-treated (indicated as red curves) cells. Regression values for the accuracy of each curve fit are indicated. Results are for the mean ± SEM for **(Aii, Bii, Cii & Dii)** the SiR-tubulin maximum fluorescence recovery in the bleached area and **(Aiii, Biii, Ciii & Diii)** the time to reach half-maximal recovery of fluorescence ($t_{1/2}$). Error bars represent the

standard error of the means and asterisks indicate values calculated to be statistically significantly different (*p≤0.05, **p≤0.01, ***p≤0.001, ****p≤0.0001 n=10 randomly selected cells. n.s.=not significant). **(Aiv, Biv, Civ & Div)** Fluorescence recovery of the GFP-DCX proteins in non-(shown as black curve) and taxol-treated (shown as green curves) SH-SY5Y cells were monitored post-bleach at 0.6 s interval for 60 s in order to study the impact of taxol-induced MT stabilization on GFP-DCX proteins dynamics. Regression values for the accuracy of each curve fit are indicated. Results are for the mean ± SEM for **(Av, Bv, Cv & Dv)** the GFP-tagged proteins maximum fluorescence recovery in the bleached area and **(Avi, Bvi, Cvi & Dvi)** the time to reach half-maximal recovery of fluorescence ($t_{1/2}$). Error bars represent the standard error of the means and asterisks indicate values calculated to be statistically significantly different (*p≤0.05, **p≤0.01, ***p≤0.001, ****p≤0.0001 n=10 randomly selected cells. n.s.=not significant).

Figure 7. DCX S28A accelerates β-actin exchange rate within the F-ACT but DCX S28E slows F-ACT dynamics. (A-C) SH-SY5Y cells were transfected to co-express GFP-vector (control), GFP-DCX WT, GFP-DCX S28A and GFP-DCX S28E with β-actin-mCherry. 2-colour FRAP protocol was performed to monitor the simultaneous recovery of GFP-tagged constructs and β-actin-mCherry. Panels in **(A)** represents the merge images of the GFP-tagged constructs and β-actin-mCherry (panels as indicated) and panels in **(B)** displays β-actin-mCherry only. Representative images in **(A)** and **(B)** are photobleached in a small ROI indicated by the white rectangle in cell images for bleach time-point and **(C)** quantitative analysis were performed for the fluorescence recovery subsequently monitored post-bleach at 0.6 s intervals for 60 s. Images are shown at 3 s interval for 60 s. regression values (R^2) of the respective curve fits are indicated. Scale bars represent 10 µm. **(D & E)** Pooled quantitative parameters derived from 2-colour FRAP imaging data for the β-actin-mCherry in association with GFP-tagged constructs and the recovery of the ROI fluorescence for β-actin-mCherry associated with GFP-DCX proteins were indicated. Results are for the mean ±SEM or **(D)** the fluorescence maximum recovery for β-actin-mCherry in the bleached areas and **(E)** the time to reach the half-maximal recovery of fluorescence ($t_{1/2}$) for β-actin-mCherry associated with GFP-DCX proteins. Error bars represent the standard error of the means and asterisks indicate values calculated to be statistically significantly different (*p≤0.05, ****p≤0.0001 n=10 randomly selected cells. n.s.= not significant). **(F)** FRAP data summary.

Figure 8. Schematic model of the impact of DCX S28A and DCX S28E. The schematic model summarizes our findings regarding the impact of DCX Ser28 mutants, DCX S28A and DCX S28E, on MTs and F-ACT. Compared to DCX WT, increased association of DCX S28A with MTs but decreased association with F-ACT and Spn are observed. Conversely, DCX S28E phosphomimetic mutant shows enhanced association with F-ACT and Spn but decreased association with MTs as well as higher tubulin exchange rate with MT networks.

Research highlights (max 85 characters including spaces per bullet point, max 5 bullet points)

- DCX S28A and S28E mutants define a reciprocal association of DCX with MTs and ACT.
- The DCX S28E mutant favours association with the adaptor protein Spn.
- Exchange rates of tubulin within MTs are accelerated in the presence of DCX S28E.
- Exchange rates of ACT are slowed in the presence of DCX SE28E.

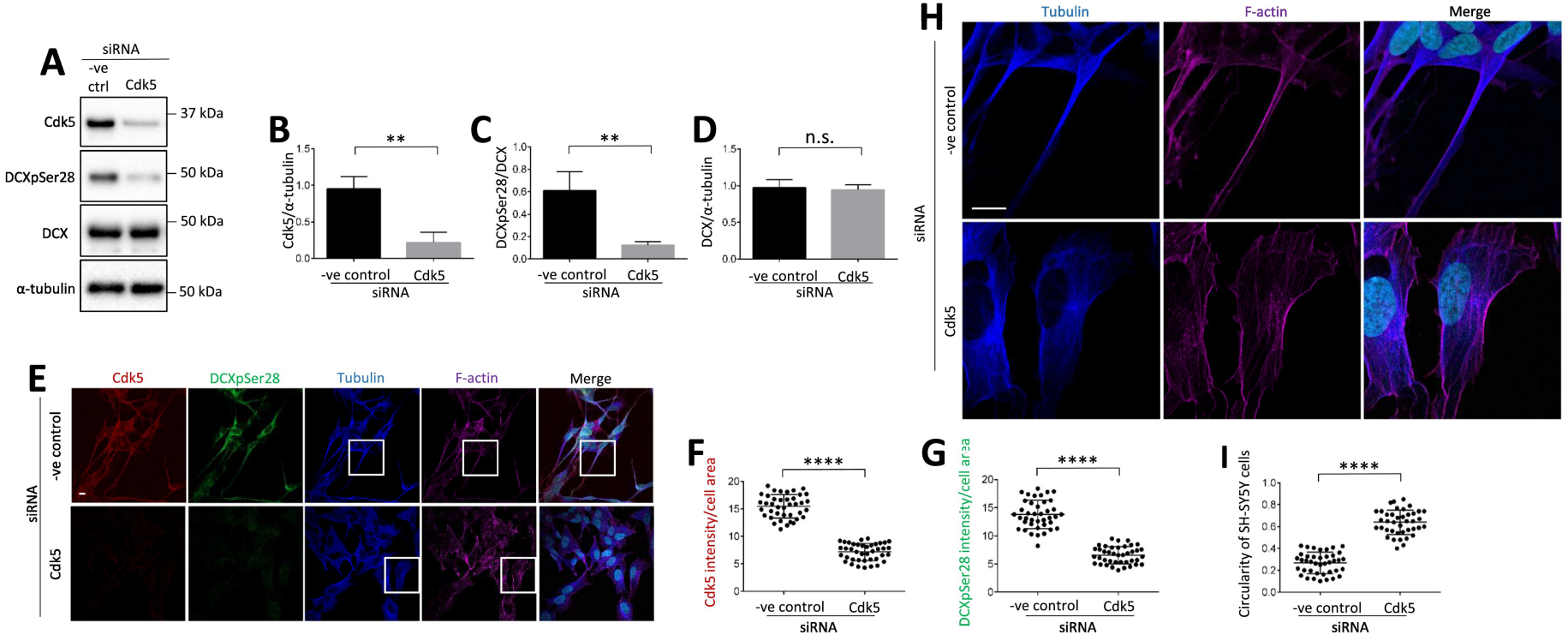
A
siRNA
-ve ctrl
Cdk5
Cdk5
DCXpSer28
DCX
α-tubulin
37 kDa
50 kDa
50 kDa
50 kDa
B
Cdk5/α-tubulin
**
-ve control
Cdk5
siRNA
C
DCXpSer28/DCX
**
-ve control
Cdk5
siRNA
D
DCX/α-tubulin
n.s.
-ve control
Cdk5
siRNA
E
Cdk5
DCXpSer28
Tubulin
F-actin
Merge
siRNA
-ve control
Cdk5
F
Cdk5 intensity/cell area
****
-ve control
Cdk5
siRNA
G
DCXpSer28 intensity/cell area
****
-ve control
Cdk5
siRNA
H
Tubulin
F-actin
Merge
siRNA
-ve control
Cdk5
I
Circularity of SH-SY5Y cells
****
-ve control
Cdk5
siRNA

Figure 1

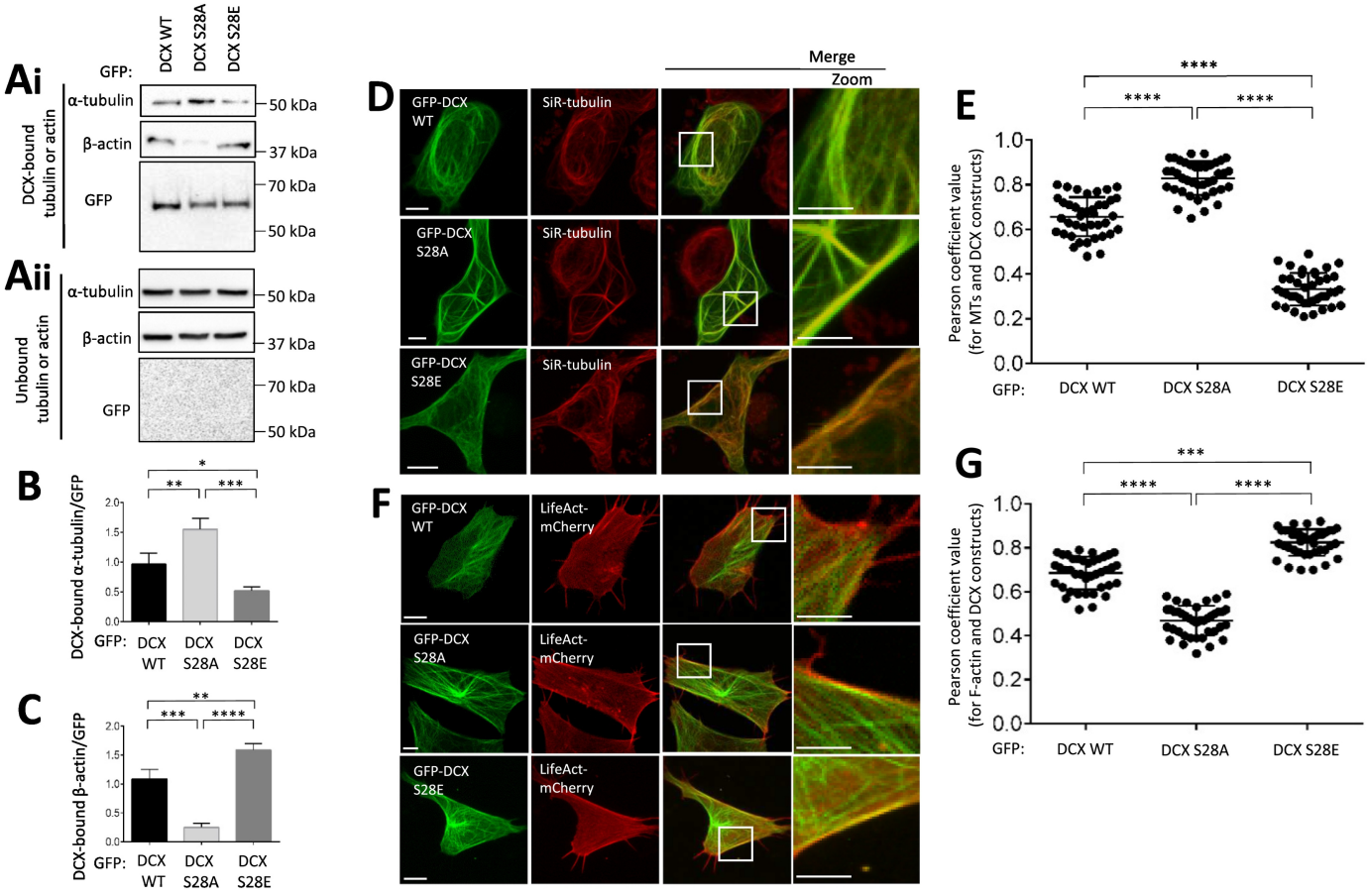
Ai
GFP:
DCX WT
DCX S28A
DCX S28E
DCX-bound tubulin or actin
α-tubulin
β-actin
GFP
50 kDa
37 kDa
70 kDa
50 kDa
Aii
Unbound tubulin or actin
α-tubulin
β-actin
GFP
50 kDa
37 kDa
70 kDa
50 kDa
B
DCX-bound α-tubulin/GFP
GFP: DCX WT DCX S28A DCX S28E
C
DCX-bound β-actin/GFP
GFP: DCX WT DCX S28A DCX S28E
D
Merge
Zoom
GFP-DCX WT
SiR-tubulin
GFP-DCX S28A
SiR-tubulin
GFP-DCX S28E
SiR-tubulin
F
GFP-DCX WT
LifeAct-mCherry
GFP-DCX S28A
LifeAct-mCherry
GFP-DCX S28E
LifeAct-mCherry
E
Pearson coefficient value (for MTs and DCX constructs)
GFP: DCX WT DCX S28A DCX S28E
G
Pearson coefficient value (for F-actin and DCX constructs)
GFP: DCX WT DCX S28A DCX S28E

Figure 2

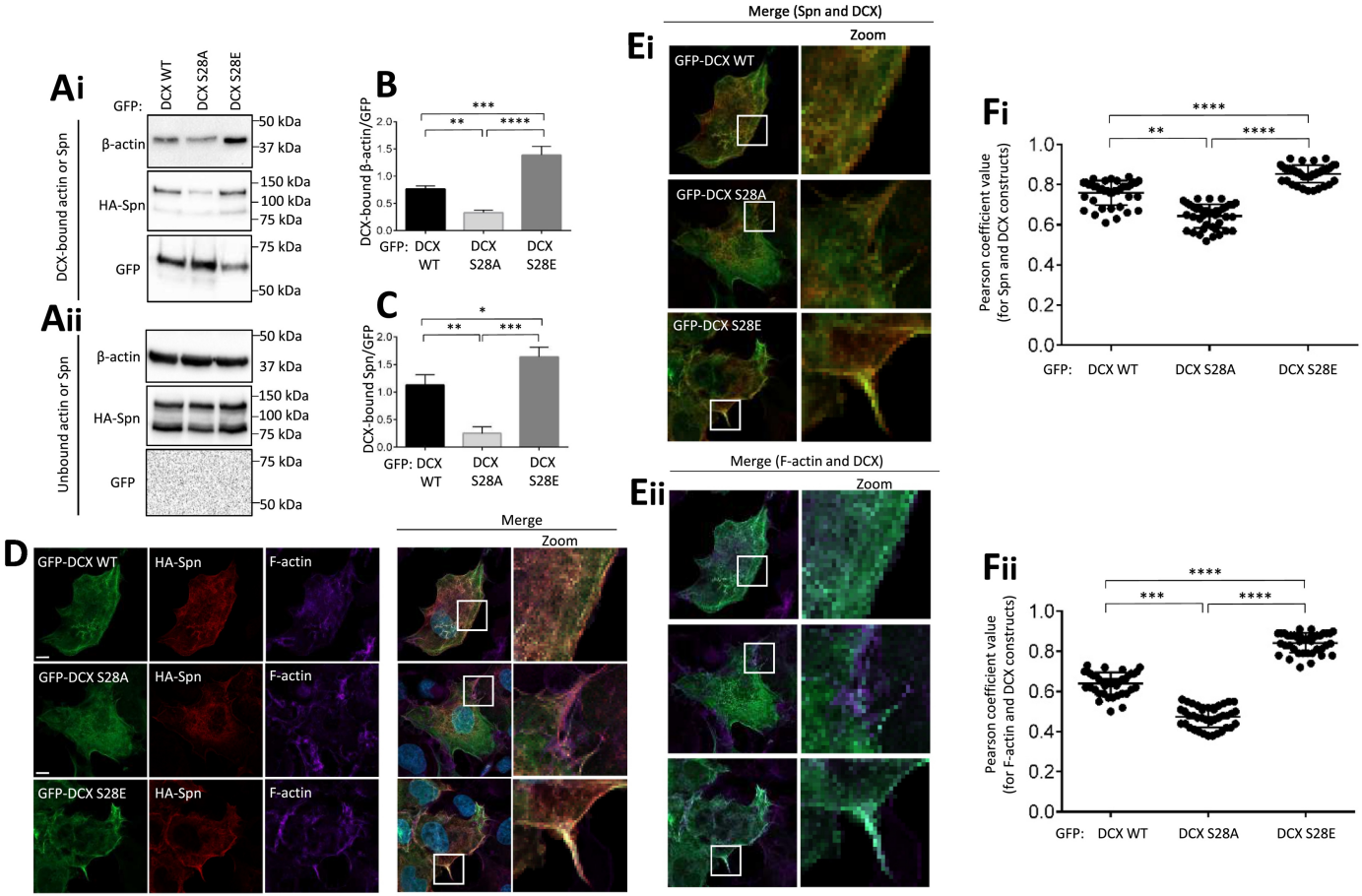
Ai
GFP:
DCX WT
DCX S28A
DCX S28E
DCX-bound actin or Spn
β-actin
HA-Spn
GFP
50 kDa
37 kDa
150 kDa
100 kDa
75 kDa
Aii
Unbound actin or Spn
B
DCX-bound β-actin/GFP
C
DCX-bound Spn/GFP
D
GFP-DCX WT
GFP-DCX S28A
GFP-DCX S28E
HA-Spn
F-actin
Merge
Zoom
Ei
Merge (Spn and DCX)
Eii
Merge (F-actin and DCX)
Fi
Pearson coefficient value (for Spn and DCX constructs)
Fii
Pearson coefficient value (for F-actin and DCX constructs)

Figure 3

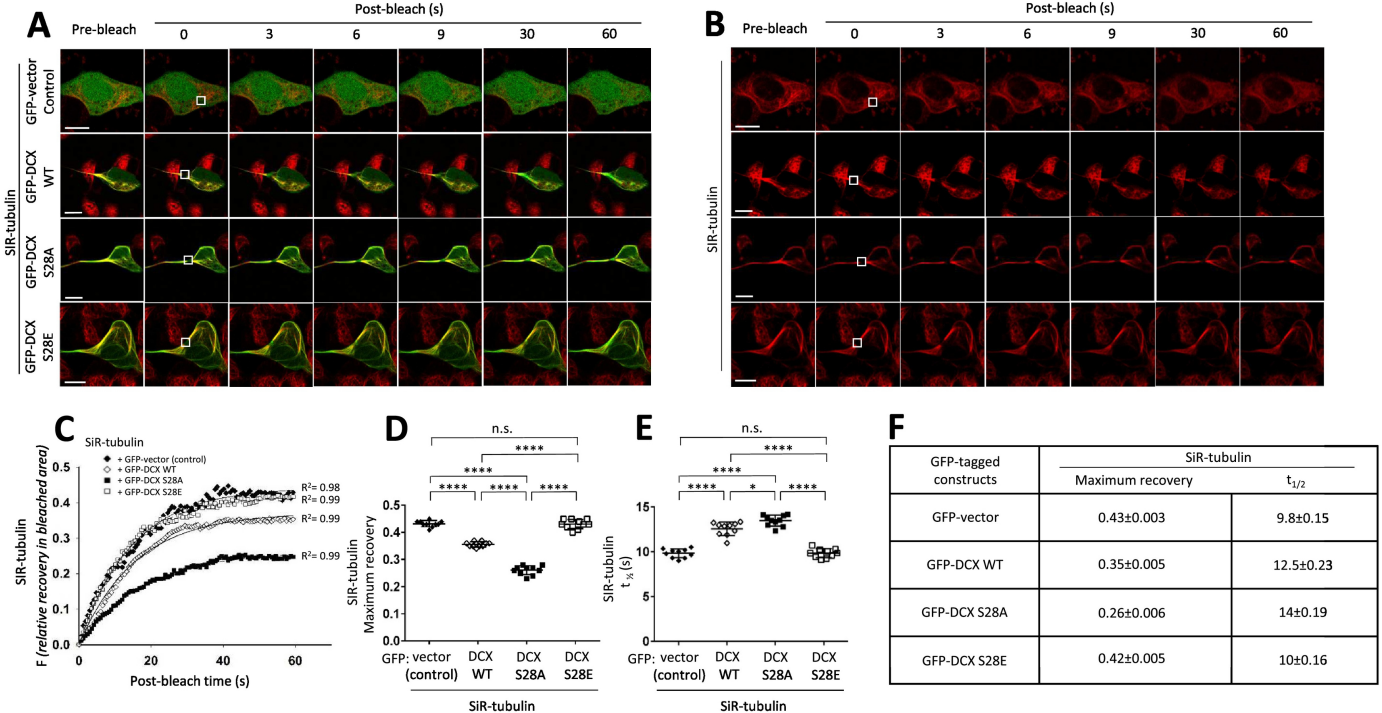

F

GFP-tagged constructs	SiR-tubulin	
	Maximum recovery	$t_{1/2}$
GFP-vector	0.43±0.003	9.8±0.15
GFP-DCX WT	0.35±0.005	12.5±0.23
GFP-DCX S28A	0.26±0.006	14±0.19
GFP-DCX S28E	0.42±0.005	10±0.16

Figure 4

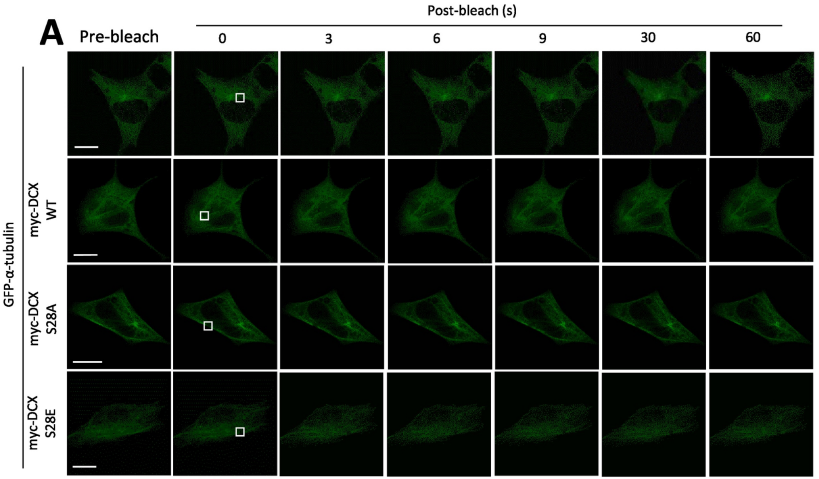

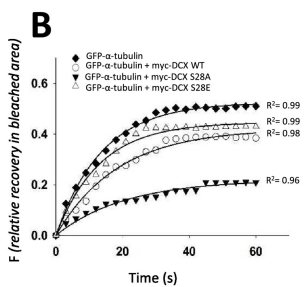

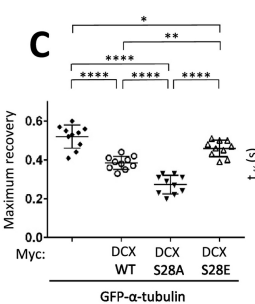

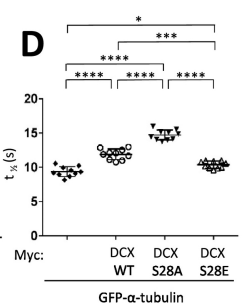

E

GFP-tagged constructs	SiR-tubulin	
	Maximum recovery	$t_{1/2}$
GFP-vector	0.52±0.018	9.37±0.22
GFP-DCX WT	0.38±0.010	11.9±0.24
GFP-DCX S28A	0.27±0.015	14.71±0.23
GFP-DCX S28E	0.45±0.013	10.37±0.16

Figure 5

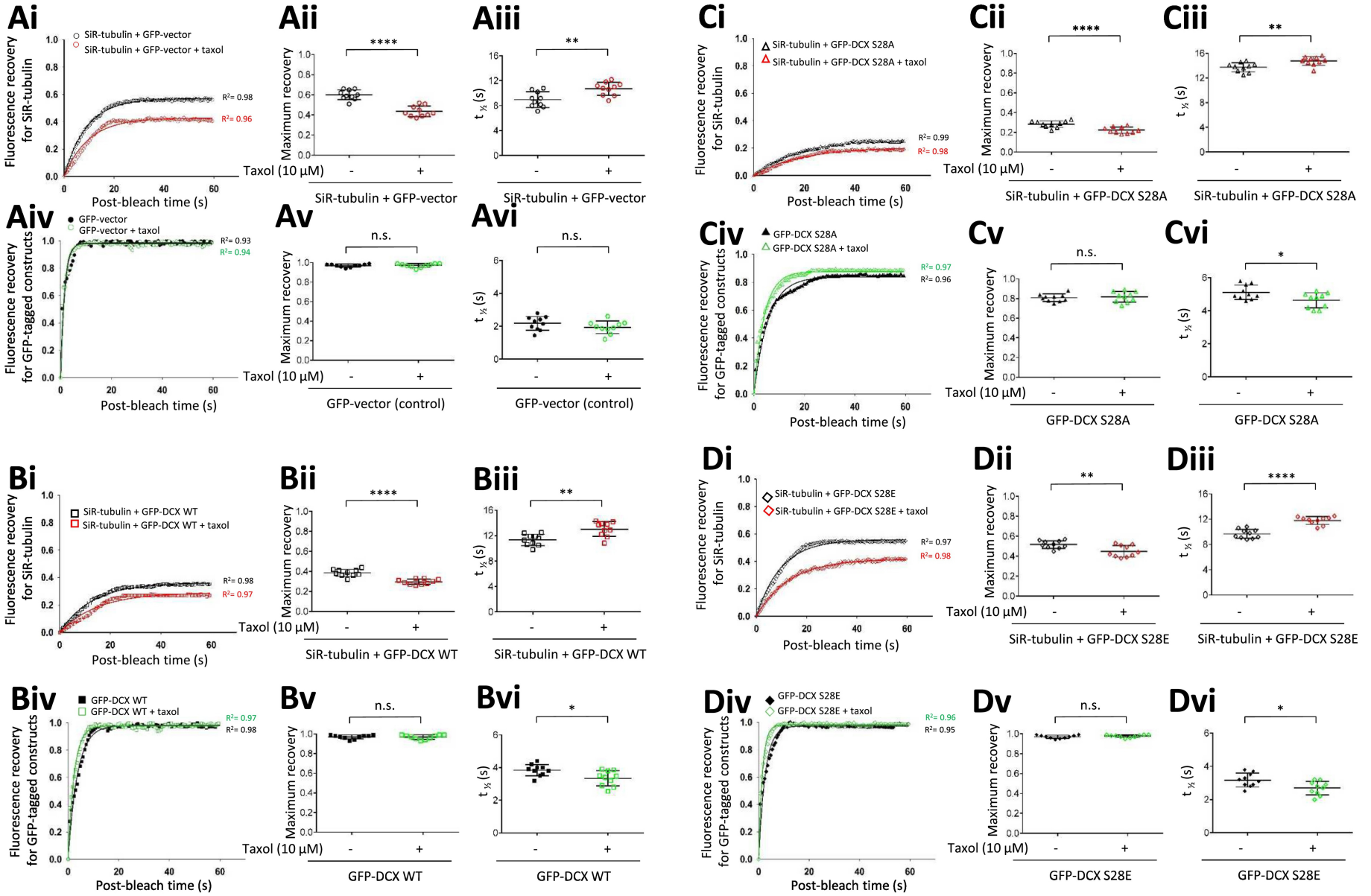
Ai
SiR-tubulin + GFP-vector
SiR-tubulin + GFP-vector + taxol
R²= 0.98
R²= 0.96
Fluorescence recovery for SiR-tubulin
Post-bleach time (s)
Aii
****
Maximum recovery
Taxol (10 μM)
SiR-tubulin + GFP-vector
Aiii
**
t ½ (s)
SiR-tubulin + GFP-vector
Aiv
GFP-vector
GFP-vector + taxol
R²= 0.93
R²= 0.94
Fluorescence recovery for GFP-tagged constructs
Post-bleach time (s)
Av
n.s.
Maximum recovery
Taxol (10 μM)
GFP-vector (control)
Avi
n.s.
t ½ (s)
GFP-vector (control)
Bi
SiR-tubulin + GFP-DCX WT
SiR-tubulin + GFP-DCX WT + taxol
R²= 0.98
R²= 0.97
Fluorescence recovery for SiR-tubulin
Post-bleach time (s)
Bii
****
Maximum recovery
Taxol (10 μM)
SiR-tubulin + GFP-DCX WT
Biii
**
t ½ (s)
SiR-tubulin + GFP-DCX WT
Biv
GFP-DCX WT
GFP-DCX WT + taxol
R²= 0.97
R²= 0.98
Fluorescence recovery for GFP-tagged constructs
Post-bleach time (s)
Bv
n.s.
Maximum recovery
Taxol (10 μM)
GFP-DCX WT
Bvi
*
t ½ (s)
GFP-DCX WT
Ci
SiR-tubulin + GFP-DCX S28A
SiR-tubulin + GFP-DCX S28A + taxol
R²= 0.99
R²= 0.98
Fluorescence recovery for SiR-tubulin
Post-bleach time (s)
Cii
****
Maximum recovery
Taxol (10 μM)
SiR-tubulin + GFP-DCX S28A
Ciii
**
t ½ (s)
SiR-tubulin + GFP-DCX S28A
Civ
GFP-DCX S28A
GFP-DCX S28A + taxol
R²= 0.97
R²= 0.96
Fluorescence recovery for GFP-tagged constructs
Post-bleach time (s)
Cv
n.s.
Maximum recovery
Taxol (10 μM)
GFP-DCX S28A
Cvi
*
t ½ (s)
GFP-DCX S28A
Di
SiR-tubulin + GFP-DCX S28E
SiR-tubulin + GFP-DCX S28E + taxol
R²= 0.97
R²= 0.98
Fluorescence recovery for SiR-tubulin
Post-bleach time (s)
Dii
**
Maximum recovery
Taxol (10 μM)
SiR-tubulin + GFP-DCX S28E
Diii
****
t ½ (s)
SiR-tubulin + GFP-DCX S28E
Div
GFP-DCX S28E
GFP-DCX S28E + taxol
R²= 0.96
R²= 0.95
Fluorescence recovery for GFP-tagged constructs
Post-bleach time (s)
Dv
n.s.
Maximum recovery
Taxol (10 μM)
GFP-DCX S28E
Dvi
*
t ½ (s)
GFP-DCX S28E

Figure 6

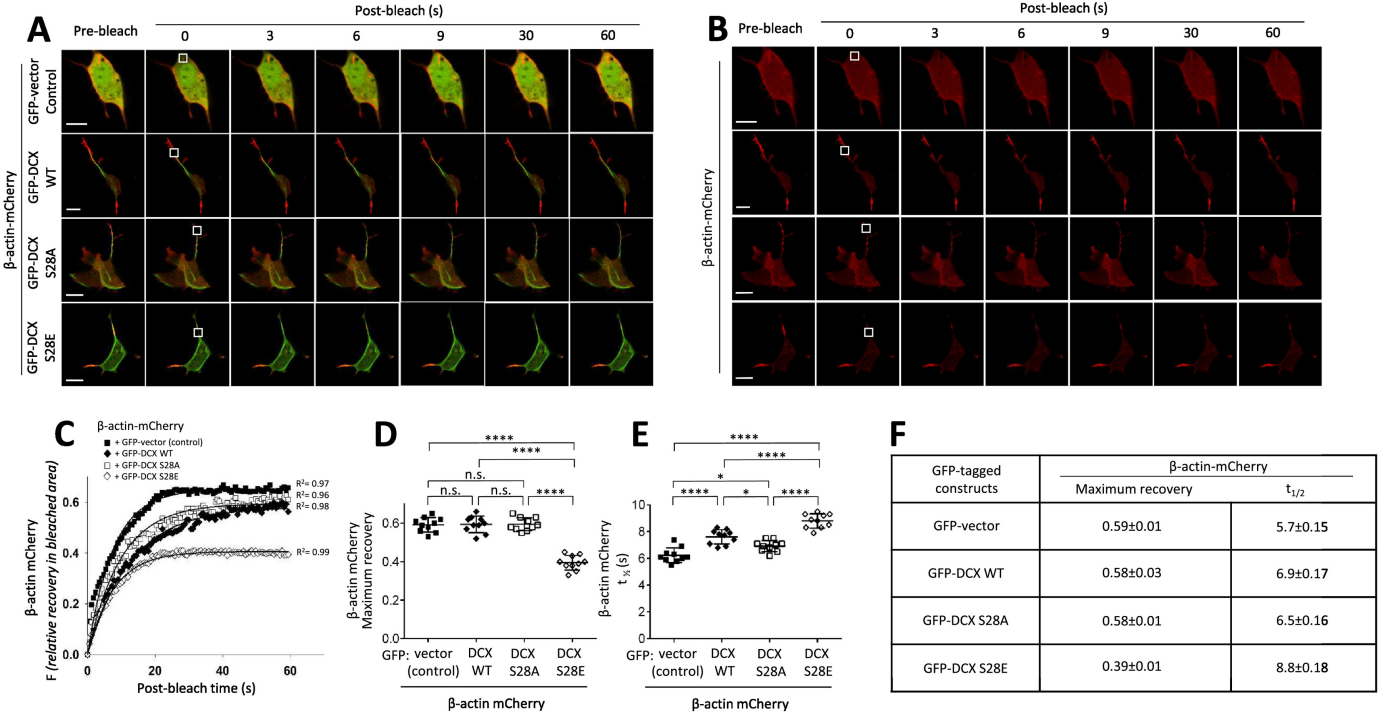

F

GFP-tagged constructs	β-actin-mCherry	
	Maximum recovery	$t_{1/2}$
GFP-vector	0.59±0.01	5.7±0.15
GFP-DCX WT	0.58±0.03	6.9±0.17
GFP-DCX S28A	0.58±0.01	6.5±0.16
GFP-DCX S28E	0.39±0.01	8.8±0.18

Figure 7

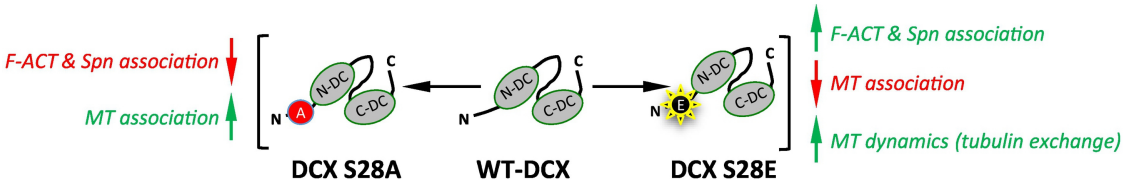
F-ACT & Spn association
MT association
N-DC
C-DC
C
N
A
E
DCX S28A
WT-DCX
DCX S28E
F-ACT & Spn association
MT association
MT dynamics (tubulin exchange)

Figure 8